Gheorghe Asachi Technical University of Iasi

Faculty of Chemical Engineering and Environmental Protection

Innovative electroluminescent nanocomposites for a new approach in polymer based light emitting devices

project: 335/5.10.2011 **Stage II** (2013)

Scientific report

Preparation of the CdSe NC's

In the investigated synthesis path, the formation of the cadmium myristate (or lauriate, stearate) complex as reaction precursor takes place "in situ". As primary cadmium source, for further formation of the required cadmium complexes, both CdO and Cd(CH3COO)2 were tested. Due the superior results in terms of emission efficiency of the synthesized CdSe QD's in case of CdO using, this path was chosen for obtaining the composite. As selenium precursor, tri-N-butylphosphine selenide (TBP-Se) was prepared. Tri-N-octylphospine (TOP) was also tested but the influence over the synthesis process is almost irrelevant, being easily attributed to the inherent experimental errors. In our attempt to avoid the use of alkylphosphines, which are toxic and expensive, in selenium precursor preparation, tri-N-butylamine was tested. The result was unsuccessful since total solvation of the selenium powder was not achieved even at elevated temperatures (150 – 170^{o}C) due the lower reactivity of the non participating electron pair of nitrogen compared with those of phosphor. CdSe NC's were prepared by a modified colloidal synthesis procedure which uses glycerin as reaction medium. In the first step the influence of selected saturated monocarboxylic fatty acids and the primary cadmium source (CdO and $(CH_3COO)_2Cd$) were investigated. The final choice of reactants used in below described typical synthesis were mainly based on the results obtained through PL emission spectra evaluation for each CdSe NC's sample obtained in each preliminary synthesis procedure. In a typical synthesis procedure, 15 mL of glycerin is added in a 100 mL three neck Schenk flask provided with a temperature controlled heating mantel and magnetic stirring. The temperature is increased to aprox. 50^{o}C when 1,1 g of myristic acid is added. After the complete meltdown of the myristic acid which occurs at aprox. 55^{o}C, a quantity of 128,41 mg CdO is slowly added in the synthesis flask under vigorous stirring. From this stage, nitrogen atmosphere is required in the synthesis flask in order to avoid unwanted degradation of the reactants. The temperature is slowly raised and then maintained to 195^{o}C until complete dissolution of the CdO is achieved. This process involves the formation of the Cd-myristate complex which is visually indicated by the color change of the reaction mass from intense reddish brown to transparent or slightly yellow. In this stage the heating is interrupted and the reaction mass is allowed to cool down to the temperature required for the Se precursor injection.

Meanwhile, the selenium precursor is prepared by dissolving at room temperature in a threaded cap vial, a quantity of 79 mg of selenium powder in 1,5 mL tri-N-butylphosphine. The process takes place in a sonic bath and considered to be completed when a clear solution is obtained. When the temperature in the synthesis flask reaches 164^{o}C the entire prepared quantity of selenium precursor is quickly added and almost immediately, the color of the mass reaction begins to change. Depending on the desired emission spectra of the prepared CdSe quantum dots, the reaction time can vary between 20 to 300 s. Then, the entire synthesis batch is quickly transferred in another flask and rapidly cooled down by sinking in an ice/water mixture for crystal growth quenching. The reaction mass is transferred in a separation funnel and maintained aprox. 30 minutes for phase separation. The lower phase containing mostly glycerin and excess fatty acid is eliminated and a quantity of 10 mL of toluene is added over the remaining phase. Further toluene washing and centrifugation operations are required in order to eliminate unreacted precursors and to achieve a narrow size distribution of the prepared CdSe QD's.

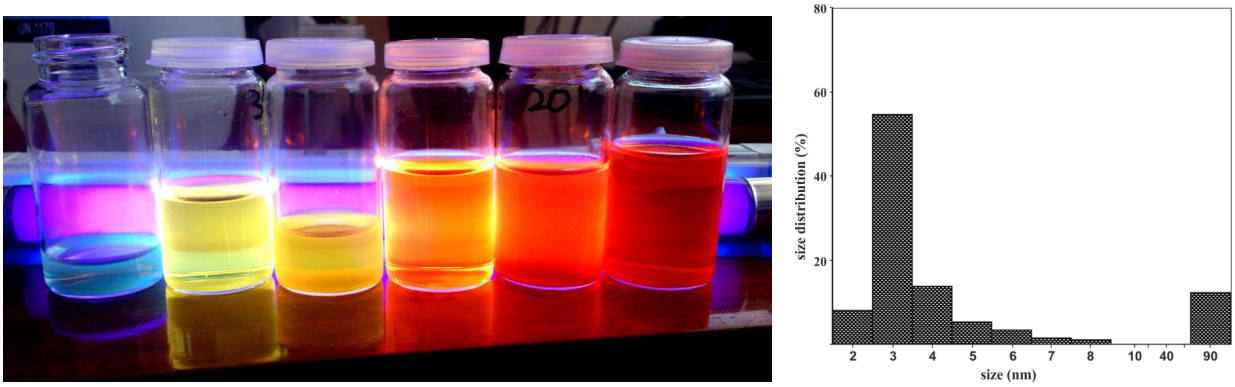

Figure 1. (left) Prepared CdSe QD's under UV excitation and (right) size distribution

2-(1H-1,2,4-Triazol-3-yl)pyridine was investigated as suitable ligand for preparation of new Y^{3+}, Sm^{3+}, Eu^{3+}, Gd^{3+} and Tb^{3+} complexes. The complexes were prepared at 1/3 metal to ligand ratio and elemental analysis, mass spectrometry, thermal analysis, FT-IR and P-XRD methods were used to investigate their structural configuration. All the prepared complexes are highly luminescent, with an impressive visual emission under UV excitation. Fluorescence spectrometry revealed in case of Sm^{3+}, $Eu^{3+}$and Tb^{3+} complexes intense metal centered specific narrow band emissions from the $f - f$ transitions within $4f$ orbitals, while in case of Gd^{3+} and Y^{3+} complexes intense wide band emissions were recorded most probable due the heavy atom effect over the excited intraligand states.

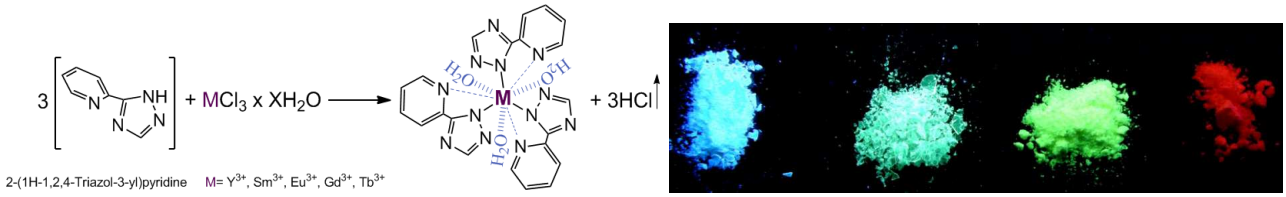

Figure 2. Reaction and structures of the ligand and prepared complexes

While the photoluminescence of all prepared complexes is quite remarkable, the mechanisms which govern their radiative transitions may be divided into two main categories. The Sm^{3+}, Eu^{3+} and Tb^{3+} prepared complexes fail in one category since their emission occurs as a "classic" metal centered (MC) luminescence with characteristic narrow emission bands arising from inner transitions within 4*f* orbitals. Since the characteristic transitions within 4*f* orbitals of Ln^{3+} cations are parity or spin forbidden, with large radiative lifetimes (10^{-3}s range) which favor radiationless deactivation and also small absorption coefficients, an appropriate ligand is required to overcome these limitations and efficiently transfer energy to the excited states of the central cation. Lanthanide luminescence is possible only in case the energy levels supplied by the excited states of the surrounding ligands to the emissive center are beyond the resonance levels specific for a certain trivalent lanthanide cation. Thus, in case of Sm^{3+} the main resonance level is $^4G_{5/2}$ (17800cm^{-1}) while in case of Eu^{3+} and Tb^{3+} the main resonance levels are $^5D_0$ (17250cm^{-1}) and $^5D_4$ (20430cm^{-1}) respectively. Generally, aromatic or hetero-aromatic compounds with conjugated π configurations with high extinction coefficients and efficient intersystem crossing transitions are suitable for a good sensitization of the lanthanide cations. In above mentioned complexes the luminescence is due a ligand to metal charge transfer (LMCT) mechanism, the sensitization induced by the 2-(1H-1,2,4-Triazol-3-yl)pyridine ligand proved to be effective for all three lanthanide cations. For the investigated complexes, the chemical structure of the ligand and also the configuration achieved through complexation could explain the efficient sensitization for all three lanthanide cations. The process may rely on an indirect sensitization through the "antenna effect" of the pyridine ring coupled to the triazole ring coordination site which subsequently transfers its excited states to the covalently bonded trivalent cation. The efficient sensitization process may be further aided by the presence of the coordinative bond between the nitrogen in the pyridine ring with the trivalent lanthanide cation. In Figure 3 (a-c) are presented excitation and emission spectra of the prepared Sm^{3+}, Eu^{3+} and Tb^{3+} complexes. The presence of the water molecules in the first coordination sphere seems to have little effect over the efficiency of the energy transfer to the central cation. Although it is well-known that the vicinity of OH oscillators favors vibrational coupling leading to non-radiative deactivation, these processes are especially efficient in aqueous solutions. Since the luminescence of the prepared complexes is achieved in their solid crystalline form, the influence of the OH oscillators is diminished to a degree which will not significantly alter the efficiency of the radiative processes.

The $[SmL_3(H_2O)_3]$ complex presents the most intense emission peak at 595 nm (Figure 3.a) due $^4G_{5/2} \rightarrow {}^6H_{7/2}$ hypersensitive transition whose intensity increases as the surrounding symmetry of the luminescent center decreases. The $^4G_{5/2} \rightarrow {}^6H_{5/2}$ and $^4G_{5/2} \rightarrow {}^6H_{9/2}$ transitions are responsible for the medium intensity peaks located at 559 and 641 nm respectively, while the lowest intensity peak located at 702 nm is due the $^4G_{5/2} \rightarrow {}^6H_{11/2}$ transition. The efficient sensitization induced by the

ligand may be additionally sustained by the presence of the $^4G_{5/2} \rightarrow {}^6H_{13/2}$ transition responsible for the 746 nm medium intensity peak at the upper edge of the NIR region. Several low intensity excitation peaks were recorded in the UV-A region between 360 -390 nm but the maximum intensity peak is located in the visible region, at 404 nm and also a lower but significant peak located at 417 nm. For this reason the $[SmL_3(H_2O)_3]$ sample was efficiently excited with a 405 nm laser diode (embedded picture in Figure 3.a) while the rest of the prepared complexes were excited with a regular UV-A fluorescent lamp.

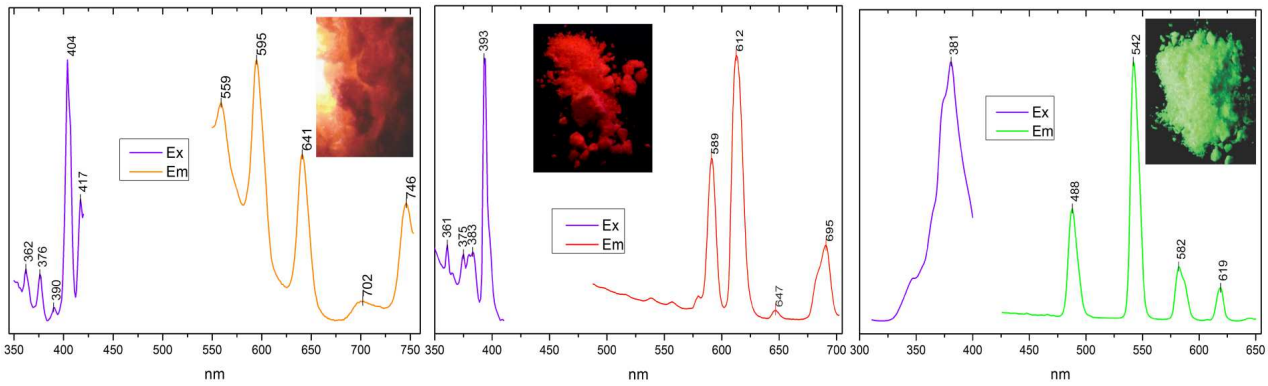

(a) (b) (c)

Figure 3. Excitation/emission spectra of prepared (a) Sm^{3+}, (b) Eu^{3+}, (c) Tb^{3+} complexes

For the $[EuL_3(H_2O)_3]$ complex (Figure 3.b) the most significant emission peaks are located at 589 and 612 nm due the $^5D_0 \rightarrow {}^7F_1$ and $^5D_0 \rightarrow {}^7F_2$ transitions The $^5D_0 \rightarrow {}^7F_1$ parity-allowed magnetic dipole transition is unaffected by the surroundings symmetry but the most intense $^5D_0 \rightarrow {}^7F_2$ electrical-dipole allowed hypersensible transition is known to be highly affected by surrounding symmetry degree. It is widely admitted that the ratio between the emission intensities of $^5D_0 \rightarrow {}^7F_2$ and $^5D_0 \rightarrow {}^7F_1$ is an asymmetry parameter for the Eu^{3+} surrounding site. As in case of $[SmL_3(H_2O)_3]$ complex, lower symmetry surroundings favor higher intensities of the hypersensible transitions. In both cases, the observations are consistent with the XRD investigations which revealed a triclinic crystallization system for the prepared complexes. The barely observable peak located at 647 nm is due the $^5D_0 \rightarrow {}^7F_3$ transition while the medium intensity peak centered at 695 nm is attributed to the $^5D_0 \rightarrow {}^7F_4$ radiative transition. All the excitation peaks were recorded in the UV-A region, with the most intense peak located at 393 nm.

In case of $[TbL_3(H_2O)_3]$ complex (Figure 3.c) the most intense emission peak is located at 542 nm due $^5D_4 \rightarrow {}^7F_5$ transition while a medium intensity peak was recorded at 488 nm due the $^5D_4 \rightarrow {}^7F_6$ transition. Both radiative transitions are practically unaffected by the symmetry of the crystalline field surroundings. The less intense 582 nm peak due the $^5D_4 \rightarrow {}^7F_4$ transition is moderately sensitive to the surroundings. The lowest intensity 619 nm peak is assigned to the $^5D_4 \rightarrow {}^7F_3$ radiative transition. The recorded excitation spectra revealed an intense broader peak located also in the UV-A region at 381 nm.

In the second main category are included the $[GdL_3(H_2O)_3]$ and $[YL_3(H_2O)_3]$ complexes whose photoluminescent properties cannot be atributed to transition within the central cation. While their recorded luminescence is strong, the characteristic emission spectra differ significantly when compared with those recorded for the complexes included in the first category. In Figure 4 (a, b) are presented excitation and emission spectra recorded for these two complexes. As could be noted, a broad emission spectrum was recorded in each case.

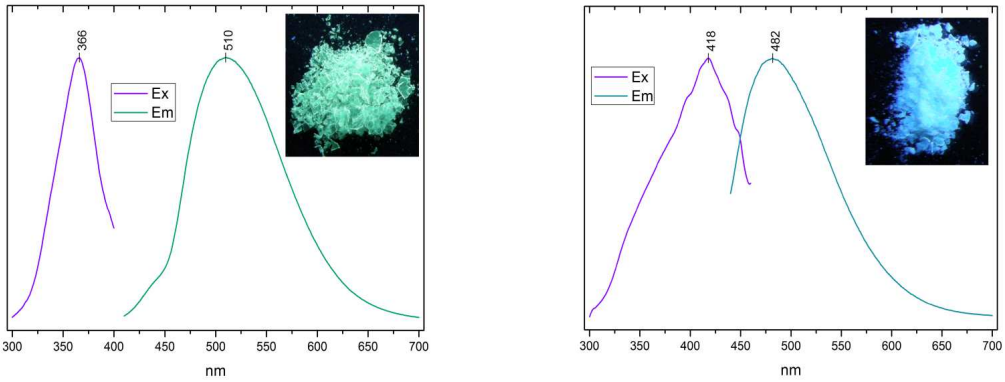

(a) (b)

Figure 4. Excitation/emission spectra of prepared (a) Gd^{3+} and (b) Y^{3+} complexes

The photoluminescence of these two complexes is rather a result of influence of the heavy cation vicinity (Gd^{3+} or Y^{3+}) over the excited states of the ligand. The Gd^{3+} cation is already known as an excellent candidate for triggering intraligand radiative processes, its paramagnetism with 7 unpaired electrons favoring intersystem crossing in ligands. Vogler and Kunkely explored in detail the role of heavy atom, especially of lanthanides, in triggering radiative processes in a series of surrounding ligands. Also their work emphasizes the role of the Gd^{3+} in achieving enhanced photoluminescent properties due the intraligand radiative processes. What is even more interesting is that the observed photoluminescence of the $[GdL_3(H_2O)_3]$ prepared in this work is in total agreement with the studies over the $Gd(tta)_3$ or $Gd(qu)_3$ chelates where the emission peaks were found at 510 nm, exactly the same value recorded for the new prepared complex (Figure 4(a)). The resemblance is further sustained by the fact, that in all cases, strong luminescence appears if only the complexes are in a solid form or incorporated in a rigid matrix due the avoidance of radiationless deactivation which is favored by a more flexible structure. For the prepared $[GdL_3(H_2O)_3]$ complex the excitation peak is located in UV-A region, at 366 nm (Figure 4.a). In case of $[YL_3(H_2O)_3]$ the processes involved in achieving the photoluminescent properties are similar but, in its case the emission peak is located at 482 nm (Figure 4(b)). The displacement at smaller wavelength compared with $[GdL_3(H_2O)_3]$ may be explained by the smaller atomic mass and ionic radius of the Y^{3+} whose influence may affect slightly different the intraligand excited states of the surrounding ligands. The recorded excitation spectra is wider compared with the Gd^{3+} complex with a peak located in the upper region of the visible spectrum, centered around 418 nm (Figure 4(b)).

Absolute photoluminescence quantum yields measurements (Table 1) place in most favorable situation the Tb^{3+} complex (32.09%), while in case of Sm^{3+} complex the lowest value was recorded (12.63%). An interesting situation is encountered in case of Y^{3+} and Gd^{3+}complexes where the measured values are comparable, supporting the proposed photoluminescence mechanism based on heavy atom influence over the excited states of the surrounding ligands. The assumption is further sustained by the lifetime measurements which in case of these two complexes are located in 3-5 ns range, with very close recorded values (3.53 ns for the Y^{3+} and 3.38 for the Gd^{3+} complexes). These nanosecond range lifetimes are typical for various organic fluorophores in which category the 2-(1H-1,2,4-Triazol-3-yl)pyridine (HL) could be included. Thus, in case of these two complexes, the role of the central cation is to trigger the radiative transitions within the surrounding ligands.

Table 1. Absolute PLQY recorded for the investigated complexes

Sample	**absolute PLQY** (%) / excitation wavelength (nm)
$[YL_3(H_2O)_3]$	**21.44** / 415
$[SmL_3(H_2O)_3]$	**12.63** / 395
$[EuL_3(H_2O)_3]$	**28.81** / 385
$[GdL_3(H_2O)_3]$	**18.09** / 365
$[TbL_3(H_2O)_3]$	**32.09** / 375

The situation is markedly different in case of Sm^{3+}, Tb^{3+} and Eu^{3+} complexes where long lifetimes (400 -500 μs range) where recorded. The values are typical for “classic” metal centered luminescence, category in which these complexes are included, as mentioned above.

Large transparent photoluminescent monoliths were prepared by embedding newly synthesized Eu(III), Tb(III) and Y(III) complexes with 2-(1H-1,2,4-Triazol-3-yl)pyridine ligand in silica matrices through a modified sol-gel process. The remarkable luminescent properties of the free complexes were preserved in silica matrix, resulting in red, green and blue monoliths (Figure 5) with a shape that may be tailored during the gelation process according to specific applications. The emission peaks are located at 612 nm for the monolithic silica embedded Eu(III) complex, at 542 nm for the monolithic silica embedded Tb(III) complex and at 482 nm respectively for the silica monolith containing the Y(III) complex. Their excellent photoluminescent properties may recommend them as photonic conversion materials in various optoelectronic applications.

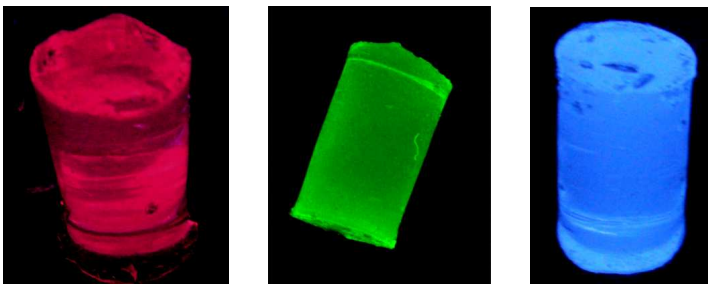

Figure 5. Prepared R, G, B monoliths

Photoluminescent silica aerogel was obtained by embedding a new Tb(III) complex in a silica matrix by using N-hydroxysuccinimide (NHSI) as ligand. The Tb(III) complex prepared at a metal to ligand ratio of 1:3 (mol%) exhibits strong photoluminescence as a result of specific radiative transitions within the Tb(III) cation with the most intense peak located at 543 nm due to 5D4 → 7F5 transition. The synthesized complex was doped in the silica matrix through a catalyzed sol-gel process. After ageing in ethanol, the alcogel was dried under supercritical regime by exchanging the ethanol with liquid carbon dioxide followed by supercritical evaporation. The leaching of the free complex from the alcogel during ageing and solvent exchange phases was found to be minimal most likely to the interactions between chemical groups of complex with those specific to silica matrix. The obtained regular shaped monolithic aerogel preserved the remarkable photoluminescent properties and also improves the thermal stability of the free complex.

SEM images recorded for the photoluminescent aerogel reinforced the conclusions provided by FT-IR, XRD and BET analysis and also the experimental observations regarding the low leaching of the complex during the solvent exchange operations requested by the aerogel preparation. Figure 6 presents SEM images recorded at 10k (a) and 50K magnification (b). Both images obtained show a typical amorphous structure for a silica aerogel in analogue conditions [6]. The image obtained at 50k magnification show a solid phase composed of clusters with average sizes of 120-150 nm weakly connected into aerogel skeletal network.

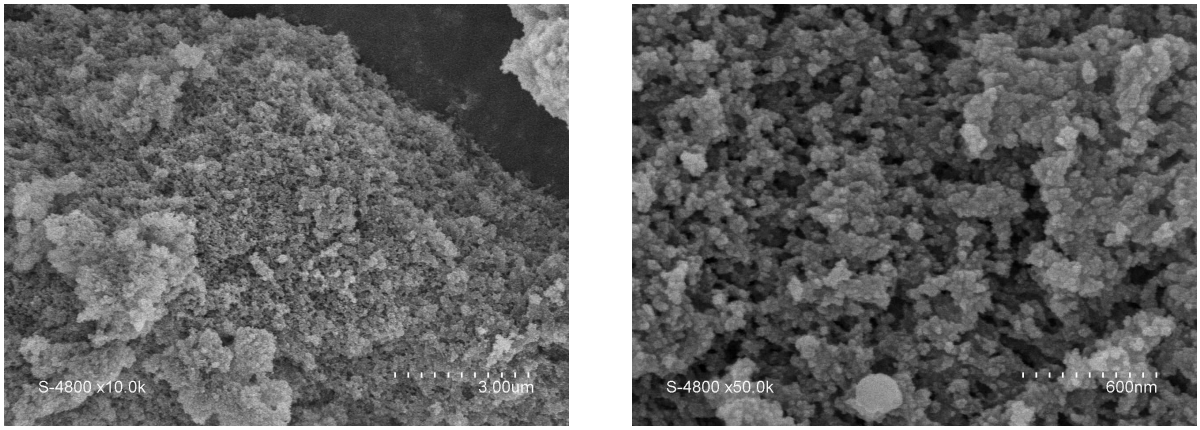

Figure 6. SEM images recorded for the photoluminescent aerogel (a) 10 k resolution (b) 50 k resolution

The macroporous structure with average pore size of 100-120 nm determined by nitrogen adsorption-desorption isotherms and BET analysis is also supported by the recorded SEM images. As can be noted, the distribution of macropores in the structure is not homogeneous, certain areas with a higher degree of aggregation being observed. This configuration suggests the presence of $[TbL_3(H_2O)_3]$ complex rather attached to the solid phase in aerogel structure than in macropores, fact which is due most likely to the interactions between chemical groups of complex with those specific to silica matrix.

The photoluminescence of the prepared aerogel is totally dependent on the properties of the embedded complex. Hence, the emission and excitation spectra recorded for the prepared aerogel are essentially the same as those recorded for the free complex. The luminescence arise from the specific inner transitions of the Ln^{3+} cations within the surrounding crystalline field, no ligand centered luminescence being detected in the recorded emission spectra. Figure 7 presents excitation and emission spectra recorded for the free complex, same spectra being recorded also for the prepared aerogel. The diagram embedded picture of the photoluminescent aerogel was taken under excitation with a 4W UV-A Philips TL4WBLB fluorescent lamp with a 360-370 nm peak emission.

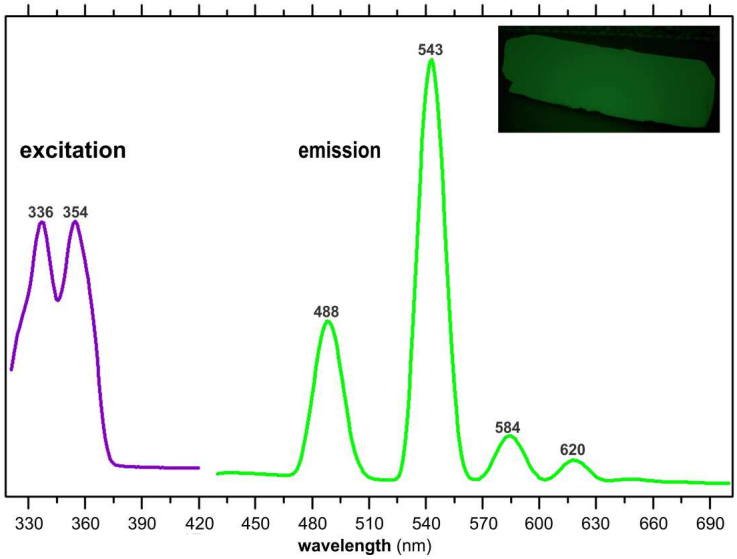

Figure 7. Excitation and emission spectra recorded for $[TbL_3(H_2O)_3]$ complex / prepared photoluminescent aerogel

Significant Tb^{3+} radiative emission peaks were recorded at 488, 543, 584 and 620 nm due to $^5D_4 \rightarrow {}^7F_6$, $^5D_4 \rightarrow {}^7F_5$, $^5D_4 \rightarrow {}^7F_4$ and $^5D_4 \rightarrow {}^7F_2$ radiative transitions. The lower intensity 584 nm peak due to $^5D_4 \rightarrow {}^7F_5$ transition is known to be moderately affected by the surroundings symmetry. The two intense emission bands centered at 488 and 543 nm are practically unaffected by the symmetry of the crystalline field surroundings. The excitation spectra recorded (Figure 7) presents two peaks centered at 336 and 354 nm. The influence of the silica matrix over the photoluminescent properties of the complex is negligible, similar spectra being recorded for the prepared aerogel. Also, the ratio between intensity of the recorded peaks is virtually identical with the case of free complex. The excitation peaks recorded for the aerogel are centered at the same wavelengths as recorded for the free complex. The only notable difference, which was also visually noted, is the lower overall emission intensity. This situation is most probable due the lower penetration of the excitation radiation in the aerogel volume to reach the embedded $[TbL_3(H_2O)_3]$ complex.

Photoluminescent polymer composites obtained through embedding two new prepared Tb(III) and Eu(III) complexes using maleimide as ligand in poly(4-styrenesulfonic acid) matrices. The photoluminescent complexes were prepared at 1:3 metal to ligand ratio.

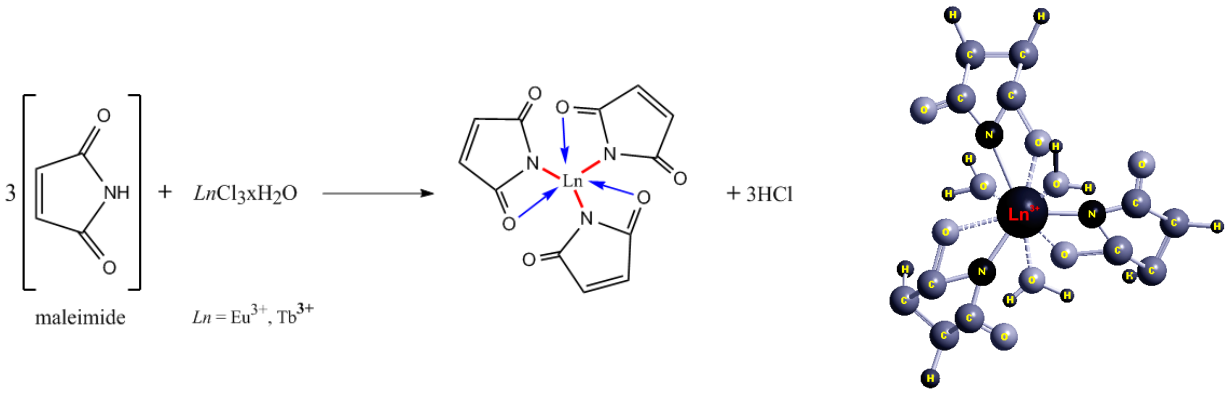

(a) **(b)**

Figure 8. Reaction involved in complexation (a) and suggested structure (b) of the prepared complexes

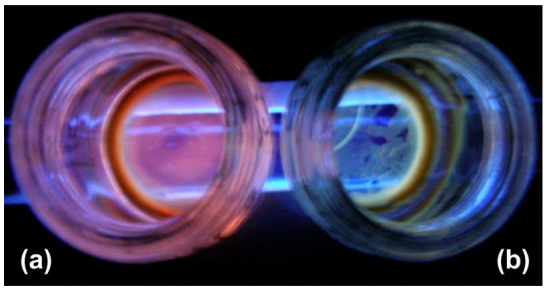

Figure 9. Prepared bulk composites with embedded (a) $[EuL_3(H_2O)_3]$, (b) $[TbL_3(H_2O)_3]$ under excitation with a UV-A fluorescent lamp

The optical properties of the prepared composites essentially rely on the photoluminescent properties of the embedded complexes. As mentioned, the main role of the PSSA polymer matrix is to provide a protective environment for the sensitive photoluminescent complexes and also to allow thin film obtaining. Both $[EuL_3(H_2O)_3]$ and $[TbL_3(H_2O)_3]$ complexes presents characteristic metal centered, narrow emission bands arising from inner transitions within 4f orbitals.

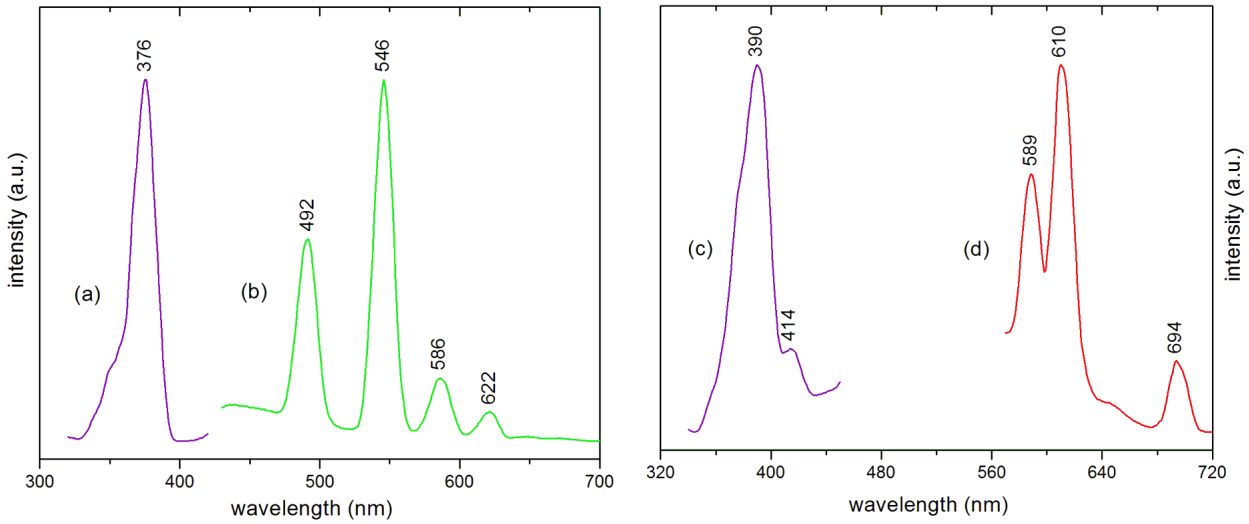

Figure 10. Recorded spectra (a) excitation, (b) emission for $[TbL_3(H_2O)_3]$ and (c) excitation, (d) emsission for $[EuL_3(H_2O)_3]$, complexes

Radiative transitions in lanthanide cations are possible when the energy levels supplied by the excited states of the surrounding ligands to the emissive center are beyond the specific resonance levels. Thus, in case of Eu^{3+} the main resonance levels are $^5D_0$ (17250 cm^{-1}) while in case of Tb^{3+} is $^5D_4$ (20430 cm^{-1}). Radiative transitions within 4f orbitals are parity or spin forbidden, with significant radiative lifetimes (10^{-3}s range). In these conditions an appropriate ligand should harvest and further supply the excited states of the central lanthanide cation with the required energy to avoid radiationless deactivation and the small absorption coefficients. In Figure 10 are presented the recorded excitation/emission spectra of the prepared $[TbL_3(H_2O)_3]$ and $[EuL_3(H_2O)_3]$ complexes. The recorded results indicate an efficient sensitization process induced by the surrounding maleimide ligands. The presence of the water molecules directly coordinated to the central lanthanide cation seems to have little or barely important effect over the efficiency of the radiative processes. Although it is well-known that the vicinity of OH oscillators favors vibrational coupling leading to non-radiative deactivation, these processes are especially efficient in aqueous solutions but in case of the prepared complexes, the luminescence is achieved in their solid crystalline form, leading to a low influence of the OH oscillators over the efficiency of the radiative processes. For both, bulk or thin film prepared composites, the recorded excitation and emission spectra are essential the same, with insignificant intensity loses due the minor influence of the PSSA matrix.

In Figure 11 are presented the micrographs recorded for PSSA-$[TbL_3(H_2O)_3]$ and PSSA-$[EuL_3(H_2O)_3]$ composites spin coated on glass slides.

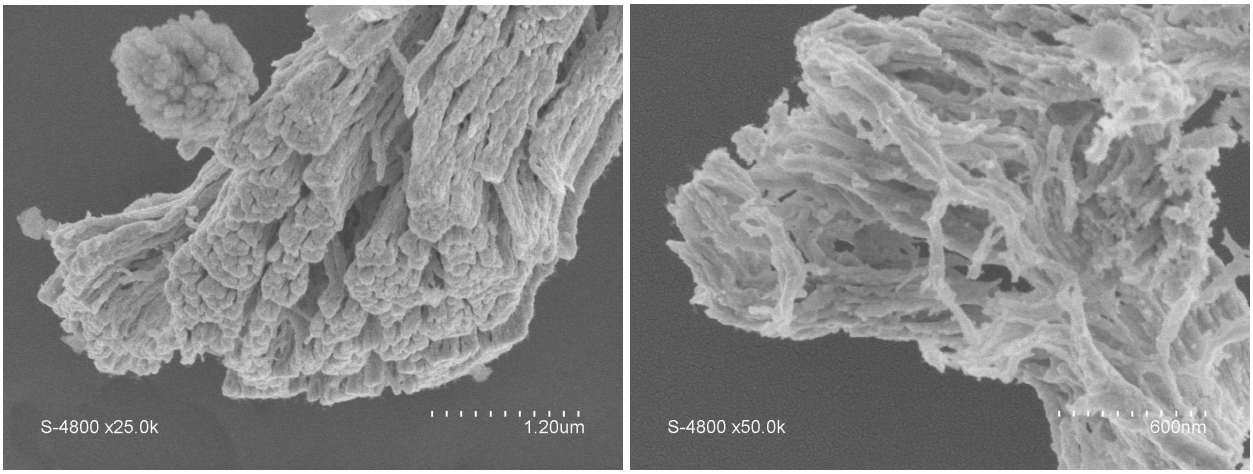

(a) **(b)**

Figure 11. SEM micrographs recorded for (a) PSSA-$[TbL_3(H_2O)_3]$ and (b) PSSA- $[EuL_3(H_2O)_3]$ composites spin coated on glass slides

Recorded SEM images revealed a filamentar arrangement of the composite on the substrate, most probable due the rapid drying processes occuring during the spin coating. Also the relative high velocity induce a preffered orientation during the crystalite formation of the complexes within the PSSA matrix. Both images suggests the existence of filamentar crystalline structures trapped

within the polymer matrix which are responsible for the photoluminescent properties of the composites.

The AFM investigation was meant to reveal the homogeneity and height variations of the photoluminescent composite films spin coated o glass slides. In Figure 12 are presented the height variations recorded in the linear exploring mode. Altough the glass substrates have their own influence, yet the detected irregularities for both spin coated composites are situated in the + 10 /- 4 nm range with a slightly better situation in case of PSSA-[$TbL_3(H_2O)_3$].

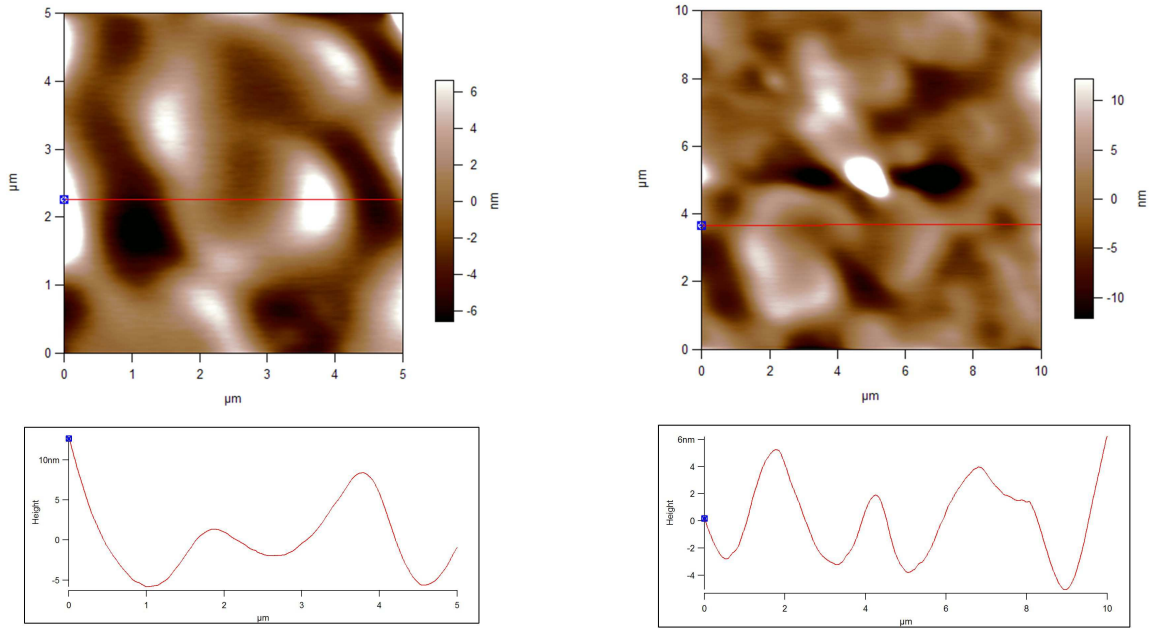

(a) **(b)**

Figure 12. Amplitude variation recorded in exploring mode for (a) PSSA- [$TbL_3(H_2O)_3$] and (b) PSSA-[$EuL_3(H_2O)_3$] composite thin films